Science
AAAS

# Hot Carrier–Assisted Intrinsic Photoresponse in Graphene

Nathaniel M. Gabor, *et al.*

*Science* **334**, 648 (2011);
DOI: 10.1126/science.1211384



*Science* (print ISSN 0036-8075; online ISSN 1095-9203) is published weekly, except the last week in December, by the American Association for the Advancement of Science, 1200 New York Avenue NW, Washington, DC 20005. 

cell operating in 1 M KBi (fig. S5A). The cell was stable for 10 hours, after which its performance gradually declined to ~80% of its initial value over 24 hours. We have found that the stability of the cell is directly related to the nature of and preparative method for the transparent conductive oxide barrier layer. For example, fluorine-doped tin oxide (FTO), when prepared and annealed on crystalline Si at high temperatures (see SOM for experimental details), results in a PEC cell with stable performance over 30 hours of testing (fig. S5B), suggesting that cells using crystalline Si with the catalysts described here have great practical value. Similar strategies may be applied for protection of the 3jn-a-Si cell; however, we note that they must be compatible with the low-temperature manufacturing conditions of 3jn-a-Si.

The integration of earth-abundant water-splitting catalysts with photovoltaic silicon cells captures the functional elements of energy capture and storage by a leaf. The ability to drive water splitting directly without the use of wires under a simply engineered configuration opens new avenues of exploration. For instance, the design described here could be adapted from a panel geometry to one based on freestanding (nano)particles in solution. Moreover, owing to the low solubility of $O_2$ and $H_2$ in water, the solar-to-fuels conversion process may be driven in the absence of a membrane. The $H_2$ produced by photochemical water splitting may be collected directly and used or combined with carbon dioxide in a synthetic liquid fuels process external to the cell. By constructing a simple, stand-alone device composed of silicon-based light absorbers and earth-abundant catalysts, the results described here provide a first step down a path aligned with the low-cost systems engineering and manufacturing (*39*) that is required for inexpensive direct solar-to-fuels systems.

**References and Notes**


1. T. R. Cook *et al.*, *Chem. Rev.* **110**, 6474 (2010).
2. J. Barber, *Phil. Trans. Roy. Soc. A* **365**, 1007 (2007).
3. T. A. Betley, Q. Wu, T. Van Voorhis, D. G. Nocera, *Inorg. Chem.* **47**, 1849 (2008).
4. N. S. Lewis, D. G. Nocera, *Proc. Natl. Acad. Sci. U.S.A.* **103**, 15729 (2006).
5. D. G. Nocera, *ChemSusChem* **2**, 387 (2009).
6. D. Abbott, *Proc. IEEE* **98**, 42 (2010).
7. O. Khaselev, A. Bansal, J. A. Turner, *Int. J. Hydrogen Energy* **26**, 127 (2001).
8. G. H. Lin, M. Kapur, R. C. Kainthla, J. O. M. Bockris, *Appl. Phys. Lett.* **55**, 386 (1989).
9. O. Khaselev, J. A. Turner, *Science* **280**, 425 (1998).
10. S. Licht *et al.*, *J. Phys. Chem. B* **104**, 8920 (2000).
11. R. E. Rocheleau, E. L. Miller, A. Misra, *Energy Fuels* **12**, 3 (1998).
12. N. A. Kelly, T. L. Gibson, *Int. J. Hydrogen Energy* **31**, 1658 (2006).
13. T. L. Gibson, N. A. Kelly, U.S. Patent 7,052,587 (2003).
14. A. E. Delahoy, S. C. Gau, O. J. Murphy, M. Kapur, J. O. M. Bockris, *Int. J. Hydrogen Energy* **10**, 113 (1985).
15. M. G. Walter *et al.*, *Chem. Rev.* **110**, 6446 (2010).
16. X. G. Zhang, *Silicon and Its Oxide* (Kluwer Academic, New York, 2001).
17. Y. W. Chen *et al.*, *Nat. Mater.* **10**, 539 (2011).
18. M. W. Kanan, D. G. Nocera, *Science* **321**, 1072 (2008).
19. Y. Surendranath, M. W. Kanan, D. G. Nocera, *J. Am. Chem. Soc.* **132**, 16501 (2010).
20. D. A. Lutterman, Y. Surendranath, D. G. Nocera, *J. Am. Chem. Soc.* **131**, 3838 (2009).
21. Y. Surendranath, M. Dincă, D. G. Nocera, *J. Am. Chem. Soc.* **131**, 2615 (2009).
22. A. J. Esswein, Y. Surendranath, S. Y. Reece, D. G. Nocera, *Energy Environ. Sci.* **4**, 499 (2011).
23. M. Risch *et al.*, *J. Am. Chem. Soc.* **131**, 6936 (2009).
24. M. W. Kanan *et al.*, *J. Am. Chem. Soc.* **132**, 13692 (2010).
25. J. Barber, *Inorg. Chem.* **47**, 1700 (2008).
26. E. M. Sproviero, J. A. Gascon, J. P. McEvoy, G. W. Brudvig, V. S. Batista, *J. Am. Chem. Soc.* **130**, 6728 (2008).
27. Y. Umena, K. Kawakami, J.-R. Shen, N. Kamiya, *Nature* **473**, 55 (2011).
28. M. D. Symes, Y. Surendranath, D. A. Lutterman, D. G. Nocera, *J. Am. Chem. Soc.* **133**, 5174 (2011).
29. J. A. Seabold, K. S. Choi, *Chem. Mater.* **23**, 1105 (2011).
30. E. M. P. Steinmiller, K. S. Choi, *Proc. Natl. Acad. Sci. U.S.A.* **106**, 20633 (2009).
31. D. K. Zhong, J. Sun, H. Inumaru, D. R. Gamelin, *J. Am. Chem. Soc.* **131**, 6086 (2009).
32. D. K. Zhong, D. R. Gamelin, *J. Am. Chem. Soc.* **132**, 4202 (2010).
33. D. K. Zhong, M. Cornuz, K. Sivula, M. Grätzel, D. R. Gamelin, *Energy Environ. Sci.* **4**, 1759 (2011).
34. X. Deng, E. A. Schiff, in *Handbook of Photovoltaic Science and Engineering*, A. Luque, S. Hegedus, Eds. (Wiley, Chichester, England, 2003), pp. 505–565.
35. Germanium commodity summary, U.S. Geological Survey; available online at http://minerals.usgs.gov/minerals/pubs/commodity/germanium/mcs-2011-germa.pdf.
36. The RHE potential is that of the standard hydrogen electrode (SHE) adjusted for the pH of the solution. Potentials (versus RHE) were calculated from the measured values (versus Ag/AgCl) according to the equation $E(\mathrm{RHE}) = E(\mathrm{Ag/AgCl}) + 0.197\mathrm{V} + (0.059\mathrm{V} \times \mathrm{pH})$.
37. Mo leaches from alloys to furnish high-surface-area materials; thus, the activity of the alloy increases with leaching time [see (*40*, *41*)]. After 9 days, leaching ceases and a very active, high-surface-area material is obtained.
38. J. J. H. Pijpers, M. T. Winkler, Y. Surendranath, T. Buonassisi, D. G. Nocera, *Proc. Natl. Acad. Sci. U.S.A.* **108**, 10056 (2011).
39. B. D. James, G. N. Baum, J. Perez, K. N. Baum, U.S. Department of Energy, Dec. 2009. Available online at: http://www1.eere.energy.gov/hydrogenandfuelcells/pdfs/pec_technoeconomic_analysis.pdf.
40. B. E. Conway, L. Bai, *Int. J. Hydrogen Energy* **11**, 533 (1986).
41. J. Z. O. Stachurski, D. Pouli, J. A. Ripa, G. F. Pokrzyk, U.S. Patent 4,354,915 (1982).


**Acknowledgments:** Sun Catalytix acknowledges Xunlight Corporation for providing the 3jn-a-Si cells and ARPA-E (DE-AR0000036) for funding. D.G.N. acknowledges support with grants from the National Science Foundation (CHE-0533150), AFOSR FA9550-09-1-0689, and the Chesonis Family Foundation. J.J.H.P. performed work as part of the Fellowships for Young Energy Scientists program of the Foundation for Fundamental Research on Matter (FOM), which is financially supported by the Netherlands Organization for Scientific Research (NWO). NWO is also gratefully acknowledged for supplying a Rubicon grant to J.J.H.P. J. Turner and E. Miller are acknowledged for helpful discussions.

**Supporting Online Material**

www.sciencemag.org/cgi/content/full/science.1209816/DC1
Materials and Methods
Figs. S1 to S5
Movie S1

15 June 2011; accepted 15 September 2011
Published online 29 September 2011;
10.1126/science.1209816

# Hot Carrier–Assisted Intrinsic Photoresponse in Graphene

**Nathaniel M. Gabor,[1] Justin C. W. Song,[1,2] Qiong Ma,[1] Nityan L. Nair,[1] Thiti Taychatanapat,[1,3] Kenji Watanabe,[4] Takashi Taniguchi,[4] Leonid S. Levitov,[1] Pablo Jarillo-Herrero[1]***

We report on the intrinsic optoelectronic response of high-quality dual-gated monolayer and bilayer graphene p-n junction devices. Local laser excitation (of wavelength 850 nanometers) at the p-n interface leads to striking six-fold photovoltage patterns as a function of bottom- and top-gate voltages. These patterns, together with the measured spatial and density dependence of the photoresponse, provide strong evidence that nonlocal hot carrier transport, rather than the photovoltaic effect, dominates the intrinsic photoresponse in graphene. This regime, which features a long-lived and spatially distributed hot carrier population, may offer a path to hot carrier–assisted thermoelectric technologies for efficient solar energy harvesting.

The photoresponse of semiconductors, which determines the performance of optoelectronic devices, is governed by energy relaxation pathways of photoexcited electron-hole pairs: Energy transferred to the lattice is lost as heat, while energy transported through charge carriers may be used to drive an optoelectronic circuit (*1*). Nanoscale systems can offer various ways to control energy relaxation pathways, potentially resulting in more efficient device operation. Novel relaxation pathways that result from electron confinement have been demonstrated in nanocrystal quantum dots and carbon nanotubes (*2*, *3*). In graphene, energy relaxation pathways are strongly altered by the vanishing electronic density of states (*4*–*6*). After initial relaxation of photoexcited carriers (as a result of electron-electron scattering and optical phonon emission), electron-lattice energy relaxation can be quenched (*4*), which creates a bottleneck that limits further energy redistribution into the lattice. With electron-to-lattice energy relaxation quenched, a novel transport regime is reached in which thermal energy is redistributed solely

[1]Department of Physics, Massachusetts Institute of Technology, Cambridge, MA 02139, USA. [2]Harvard School of Engineering and Applied Sciences, Harvard University, Cambridge, MA 02138, USA. [3]Department of Physics, Harvard University, Cambridge, MA 02138, USA. [4]National Institute for Materials Science, Namiki 1-1, Tsukuba, Ibaraki 305-0044, Japan.

*To whom correspondence should be addressed. E-mail: pjarillo@mit.edu

among electronic charge carriers. The photogenerated carrier population remains hot while the lattice stays cool.

In graphene, hot carriers should play a key role in optoelectronic response (*6*), yet measurements have not clearly determined the photocurrent generation mechanism. Numerous initial studies suggested that photocurrent generated at graphene-metal contacts (*7*–*11*) results from the photovoltaic (PV) effect, in which a built-in electric field accelerates photogenerated charge carriers to the electronic contacts. More recent studies have looked at monolayer-bilayer interfaces (*12*) and highly controlled chemical potential gradients at gate voltage–controlled p-n interfaces (*13*), and their results indicate that photothermoelectric (PTE) effects may play an important role. The PTE effect arises from a light-induced temperature difference resulting in a thermoelectric voltage. Although PTE physics has been invoked to explain photocurrent measured in graphene (*12*, *13*), an experimental proof of its role in determining the intrinsic photoresponse has been lacking.

We report optoelectronic measurements of dual gate voltage–controlled graphene p-n junction devices in the presence of local laser excitation. Dual gate control allows us to explore the rich structure of photoresponse as a function of carrier polarity, varied independently in two adjacent regions. Our measurements indicate that hot electronic carriers dominate graphene's intrinsic optoelectronic response at temperatures ranging from room temperature down to 10 K and in the linear optical power regime. The hot carrier regime manifests as a strong PTE effect that results in a striking six-fold photovoltage pattern as a function of gate voltages. Additionally, the spatial and charge density dependence of the photoresponse establishes a strong connection between thermal energy transport and electronic charge carriers.

We studied p-n junctions in both monolayer and bilayer graphene devices integrated with global bottom gates and local top gates, as shown in Fig. 1A and described in (*14*). Tuning the bottom- and top-gate voltages, $V_{BG}$ and $V_{TG}$ respectively, allows independent control of carrier density of electrons (n-type carriers) and holes (p-type carriers) in each region (*15*–*17*). By applying voltages of opposite polarity on $V_{BG}$ and $V_{TG}$, we formed a p-n junction at the interface of p- and n-type regions in a single graphene sample (Fig. 1C, bottom). The gate configurations in our devices are similar to those in (*15*–*17*), with p-n junctions estimated to be narrower than ~80 nm.

We first characterized our devices via electronic transport measurements of resistance $R$ as a function of $V_{BG}$ and $V_{TG}$. Figure 1B shows $R$ versus $V_{BG}$ and $V_{TG}$ for a monolayer graphene (MLG) p-n junction. The resistance exhibited four characteristic regions, a distinctive behavior that reflects gate voltage–tunable charge density and a sharp density gradient at the p-n interface (*15*–*17*). When the charge density $n_c$ was tuned near the neutrality point in each gated region, $R$ increased because of the low density of conduction carriers. When two gates were present, this resulted in two intersecting lines of relatively high resistance, and a maximum resistance $R_{max}$ at their intersection, the global charge neutrality point (CNP). The two lines divided the resistance map into four regions: p-n, n-n, n-p, and p-p, labeled according to the carrier doping induced in the bottom-gated and dual-gated regions (regions 1 and 2, respectively). As the carrier density increased away from the CNP, the resistance decreased monotonically from $R_{max}$.

Devices were placed in a low-temperature optical cryostat that combined electronic transport with mirror-controlled scanning laser excitation (Fig. 1C and fig. S1). Figure 1D shows a photocurrent image obtained by scanning a focused laser spot 1 μm in diameter (λ = 850 nm) over the device at $V_{SD}$ = 0 V while measuring the current $I$. At the sharply defined junction, we observed a strong photocurrent that was an order of magnitude greater than the photocurrent at the contacts and increased linearly with optical power. The maximum photocurrent responsivity reached 5 mA/W at low temperatures, which is greater than previously reported values of 1 mA/W at room temperature (*10*, *13*). As a function of distance, the photocurrent exhibited a triangular shape centered at the junction and extending several micrometers to the contacts (solid line in Fig. 1E). A triangular profile indicates that the charge carriers remained hot throughout the device and contributed to photocurrent (see below).

Unlike the resistance measurements, in which we observed four gate voltage regions, optoelectronic measurements with the laser fixed at the junction exhibited a striking photovoltage pattern, with six regions of alternating photovoltage sign as a function of $V_{BG}$ and $V_{TG}$ (Fig. 2). Because the photoconductance in graphene is negligible (*9*), the photovoltage established across the device can be determined from the measured $I_{PH}$ according to the relation $V_{PH} = I_{PH}R$. If the photocurrent originates from the PV effect, in which the photovoltage is proportional to the electric field induced at the junction, then we would

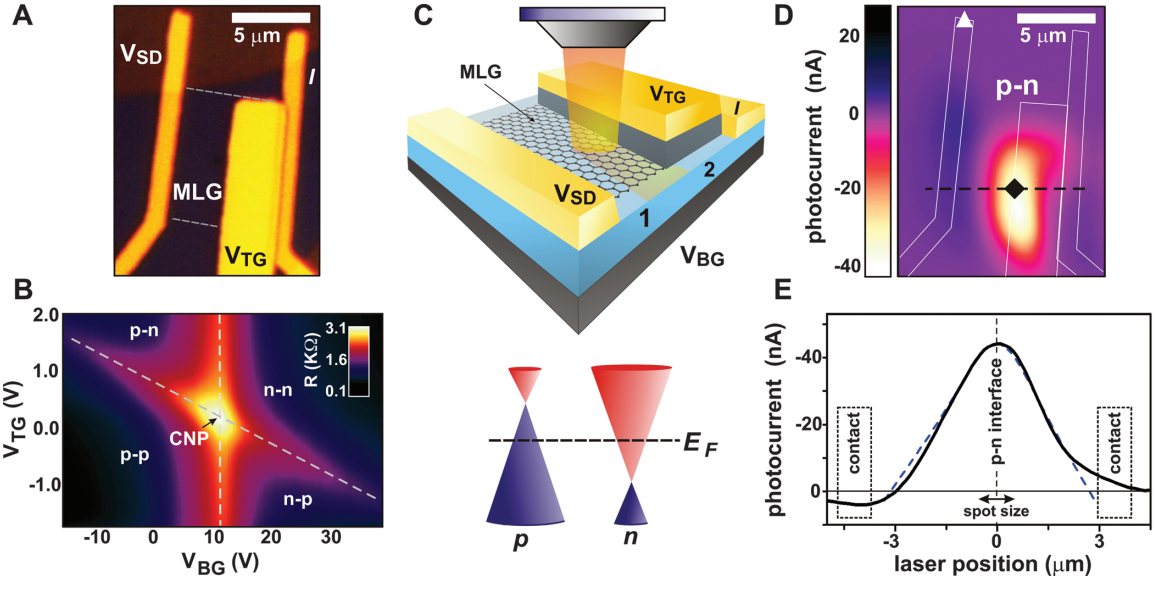


**Fig. 1.** Device geometry, band structure, and optoelectronic characteristics of the graphene p-n junction. (**A**) Optical microscope image of the dual-gated device incorporating boron nitride top-gate dielectric. The current $I$ is measured at fixed bias voltage $V_{SD}$. Dashed white lines mark the boundaries of graphene. MLG, monolayer graphene; $V_{TG}$, top-gate voltage. (**B**) Resistance (in kilohms) versus $V_{BG}$ and $V_{TG}$ at $V_{SD}$ = 1.4 mV and $T$ = 175 K. Four regions are labeled according to carrier doping, p-type or n-type, in the bottom- and top-gated regions, respectively. CNP, charge neutrality point. (**C**) Experimental schematic (top) and schematic of monolayer graphene's band structure in the p-n junction (bottom), showing electron bands (blue) and hole bands (red). The dashed line represents the electron chemical potential (or Fermi energy) $E_F$. (**D**) Spatially resolved photocurrent map at $T$ = 40 K with laser wavelength λ = 850 nm and optical power = 50 μW ($V_{BG}$ = −5 V, $V_{TG}$ = 2 V, $V_{SD}$ = 0 V). White lines mark location of gold contact and gate electrodes; white triangle is measurement point for Fig. 2A. (**E**) Photocurrent line trace taken at dashed line in (D). Laser position = 0 corresponds to the edge of the top-gate electrode; the dashed line is a fit to the data (see text).

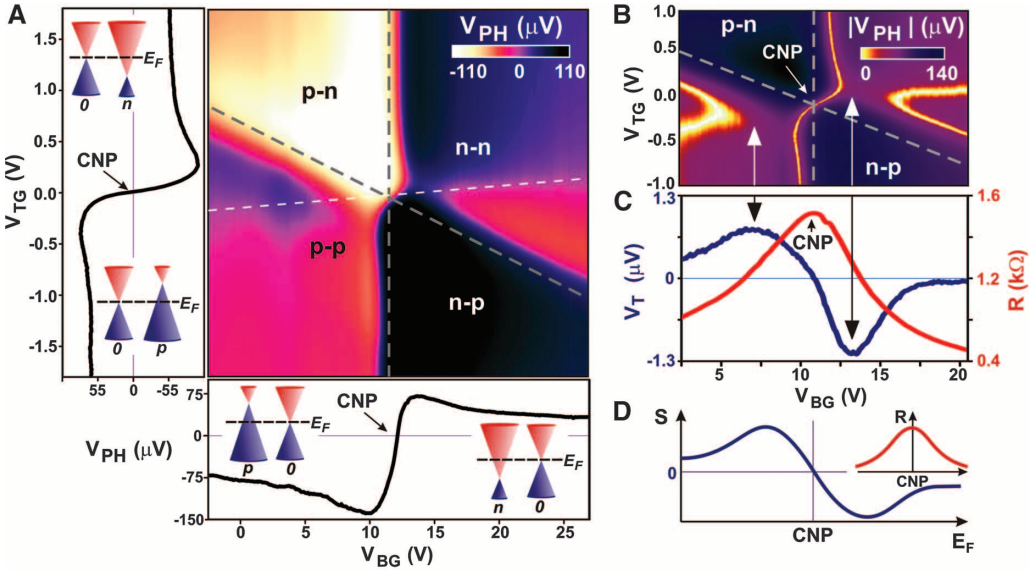


**Fig. 2.** Photovoltage and thermoelectric response of the graphene p-n junction. (**A**) Photovoltage ($V_{PH}$) versus $V_{BG}$ and $V_{TG}$ at $T$ = 40 K, measured at the location marked by the triangle in Fig. 1D. Gray dashed lines are lines of high resistance from transport characteristics. The white dashed line is described in the text. Photovoltage line traces were taken along the vertical (left) and diagonal (bottom) gray dashed lines. (**B**) Absolute value of photovoltage near the CNP. (**C**) Resistance and thermovoltage versus $V_{BG}$ at $V_{SD}$ = 0 V, $V_{TG}$ = 2.0 V, and $T$ = 40 K (optical power = 1 mW, laser at triangle in Fig. 1D). (**D**) Schematic of the Seebeck coefficient as a function of Fermi energy for typical resistance characteristics of graphene (inset).

expect only a single photovoltage sign change and a monotonic dependence on increasing charge density. However, $V_{PH}$ as a function of $V_{BG}$ and $V_{TG}$ (Fig. 2A) exhibited multiple sign changes (*6*). Moreover, the photovoltage line traces extracted along the high-resistance ridges (gray lines), along which charge density increases away from the CNP, exhibited strong nonmonotonic gate voltage dependence (Fig. 2A, left and bottom).

The shape of the photovoltage node lines (i.e., lines at $V_{PH}$ = 0) indicates that whereas $R$ decreased monotonically away from $R_{max}$ at the CNP, the photovoltage showed nonmonotonic dependence on gate voltages. In the PV effect, changing the direction of the electric field as the relative carrier densities are changed in regions 1 and 2 would change the sign of the photovoltage across a single nodal line. This line, along which the carrier density in the two regions is equal (white dashed line in Fig. 2A), divides the p-p and n-n regions (*6*). Figure 2B shows the photovoltage nodes determined by plotting the absolute value of photovoltage |$V_{PH}$| versus $V_{BG}$ and $V_{TG}$. We observed three photovoltage nodes that deviated substantially from lines of high resistance. Near the CNP, where $R$ decreased monotonically away from $R_{max}$, the photovoltage displayed a vertically oriented Z-shaped nodal line and two points toward which the three nodal lines converged (arrows in Fig. 2B).

Such nonmonotonic behavior of transport properties is reminiscent of the sign change and nonmonotonic charge density dependence of thermoelectric voltage in graphene (*18*–*21*). Thermoelectric transport measurements on the same sample showed that the thermovoltage $V_T$ measured as a function of $V_{BG}$ exhibited features similar to the photovoltage nodes along the high-resistance ridges. By laser-heating the gold contact far from the graphene-metal junction (triangle in Fig. 1D),we introduced a fixed uncalibrated temperature gradient across the device and measured the resulting thermovoltage (fig. S2). Figure 2C shows $V_T$ and $R$ as a function of $V_{BG}$. Whereas $R$ decreased monotonically away from the CNP, $V_T$ exhibited a nonmonotonic gate voltage dependence with peaks that corresponded closely to the gate voltages at which the three nodal lines of the photovoltage converged near the CNP (arrows in Fig. 2B).

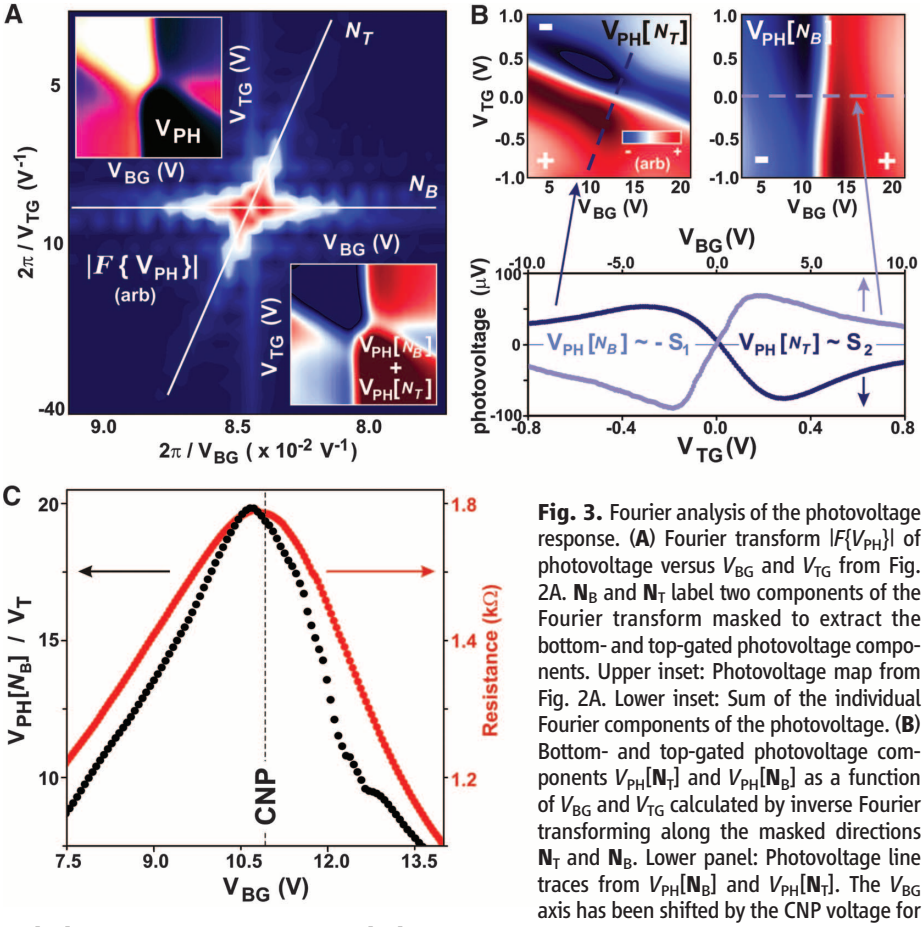


**Fig. 3.** Fourier analysis of the photovoltage response. (**A**) Fourier transform |$F\{V_{PH}\}$| of photovoltage versus $V_{BG}$ and $V_{TG}$ from Fig. 2A. $\mathbf{N_B}$ and $\mathbf{N_T}$ label two components of the Fourier transform masked to extract the bottom- and top-gated photovoltage components. Upper inset: Photovoltage map from Fig. 2A. Lower inset: Sum of the individual Fourier components of the photovoltage. (**B**) Bottom- and top-gated photovoltage components $V_{PH}[\mathbf{N_T}]$ and $V_{PH}[\mathbf{N_B}]$ as a function of $V_{BG}$ and $V_{TG}$ calculated by inverse Fourier transforming along the masked directions $\mathbf{N_T}$ and $\mathbf{N_B}$. Lower panel: Photovoltage line traces from $V_{PH}[\mathbf{N_B}]$ and $V_{PH}[\mathbf{N_T}]$. The $V_{BG}$ axis has been shifted by the CNP voltage for $V_{PH}[\mathbf{N_B}]$. (**C**) Ratio of the photovoltage $V_{PH}[\mathbf{N_B}]$ to the thermovoltage $V_T$, and resistance as a function of $V_{BG}$ measured along the white dashed line in Fig. 2A.

We attribute the intricate photovoltage pattern in graphene to the PTE effect. After optical excitation, electron-hole pairs decay rapidly (~10 to 150 fs) into a thermal distribution of electronic carriers (*22*, *23*) with a local effective temperature $T_{el}$ that remains out of equilibrium with the lattice. The difference in temperature with its

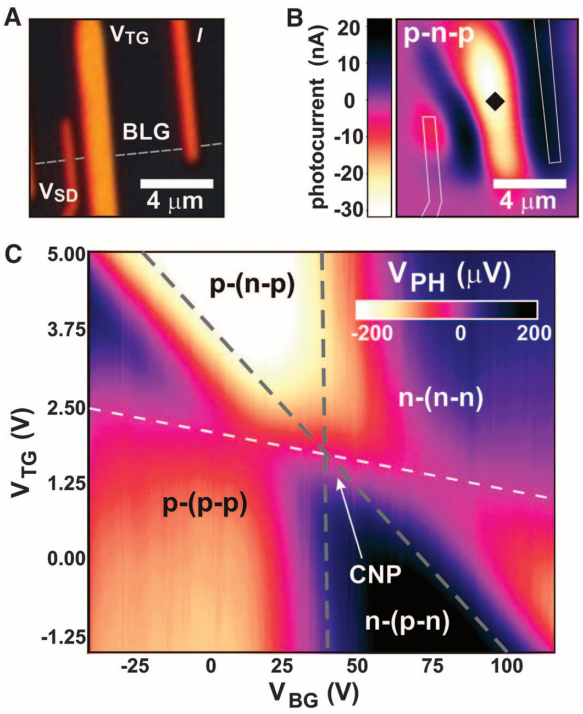


**Fig. 4.** Photoresponse in the bilayer graphene p-n-p photodetector. (**A**) Optical microscope image of the BLG device. The current $I$ is measured at fixed bias voltage $V_{SD}$. White dashed line marks the boundary of BLG. (**B**) Photocurrent map at $T$ = 40 K, $\lambda$ = 850 nm, and optical power = 200 μW ($V_{BG}$ = 15 V, $V_{TG}$ = 10 V, $V_{SD}$ = 0 V). White lines indicate location of gold contact electrodes. (**C**) Photovoltage at the n-p junction [diamond in (B)] versus $V_{BG}$ and $V_{TG}$ at $T$ = 40 K. Gray dashed lines are lines of high resistance taken from transport characteristics. White dashed line is as in Fig. 2A.

surroundings results in a thermal current that is accompanied by a charge current, the magnitude and sign of which is sensitive to carrier type and density (i.e., a p-type sample exhibits charge current with an opposite sign to that of an n-type sample). In unbiased homogeneous graphene, an isotropic thermal current flowing away from the excitation spot is not accompanied by a similar isotropic charge current.

However, in a p-n junction this symmetry is broken, and photoexcitation can result in nonzero net PTE current. The sign and magnitude of PTE voltage resulting from this current depends on the Seebeck coefficient (*12*, *24*) in each region and can be written as

$$V_{PTE} = (S_2 - S_1)\Delta T \qquad (1)$$

where $S$ is thermoelectric power (Seebeck coefficient) in the bottom- and dual-gated regions, and $\Delta T$ taken at the junction is proportional to the electron temperature difference between the area of optical excitation and its surroundings (*6*). From the Mott formula (*24*), we can write $S$ as

$$S = \frac{\pi^2 k_B^2 T}{3e} \frac{1}{R} \frac{dR}{dV_G} \frac{dV_G}{dE}\bigg|_{E = E_F} \qquad (2)$$

where $T$ is the sample temperature, $k_B$ is the Boltzmann constant, and $E_F$ is the Fermi energy (*12*, *18*–*21*). Whereas $R$ decreased monotonically with $V_G$ away from the CNP, $S$ changed nonmonotonically (Fig. 2D). The nonmonotonic dependence of $S_1$ and $S_2$ resulted in multiple sign reversals for the quantity ($S_1 - S_2$), which occurred along three nodal lines and gave rise to the six-fold pattern (Fig. 2A) (*6*), characteristic of a PTE effect in graphene.

We obtained more direct insight into the origin of the six-fold photovoltage patterns by extracting the two components of the PTE voltage individually. A Fourier analysis technique (*14*) can extract $S_1$ and $S_2$ because they depend on different combinations of $V_{BG}$ and $V_{TG}$. The Fourier transform of the data (Fig. 3A), exhibited a pair of streaks. The orientations of these streaks, horizontal ($\mathbf{N}_B$) and diagonal ($\mathbf{N}_T$), are described by the capacitance matrix of regions 1 and 2 [see (*25*)]. The relations between these streaks and the individual properties of the two regions are clarified by masking one of the streaks and performing an inverse Fourier transform of the other streak. This procedure revealed two contributions, each behaving as a function of density in the corresponding regions, $V_{PH}[\mathbf{N}_B]$ and $V_{PH}[\mathbf{N}_T]$ (Fig. 3B, top). Furthermore, the nonmonotonic density dependence of each contribution was similar to the behavior of the Seebeck coefficient given by the Mott formula (Fig. 3B, bottom). The sum $V_{PH}[\mathbf{N}_B] + V_{PH}[\mathbf{N}_T]$ reproduces the photovoltage pattern (Fig. 3A, lower inset). The nonmonotonic behavior of each term produced polarity reversal on three nodal lines and gave rise to a six-fold pattern.

Six-fold patterns were also observed in the bilayer graphene (BLG) photoresponse. Composed of two Bernal-stacked sheets of monolayer graphene, BLG has hyperbolic bands that touch at zero energy, resulting in the absence of a band gap (*26*–*28*). Figure 4 shows the photoresponse of a BLG p-n junction photodetector. Using a top-gated configuration, two back-to-back junctions could be tuned by gate voltages. The resistance behaves similarly to the MLG junction, showing four gate voltage regions separated by lines of high resistance (gray dashed lines in Fig. 4C) (fig. S3). A strong photoresponse was observed in the p-n-p configuration, with photocurrent that peaked at the p-n junctions formed near the top-gate edge (Fig. 4B). The six-fold pattern in photovoltage versus $V_{BG}$ and $V_{TG}$ indicates the presence of a strong PTE effect (Fig. 4C).

The hot carrier–assisted photoresponse in graphene is characterized by a long-lived and spatially distributed hot electronic population resulting from local excitation. The PTE photoresponse (Eq. 1) depends directly on the electronic temperature, which can be strongly enhanced by long cooling times $\tau$. Because the cooling length $\xi \propto \tau^{1/2}$ (*24*), long cooling times manifest as long cooling lengths. Using solutions to the heat equation (*14*), we fitted the photocurrent profile (dashed line in Fig. 1E) and obtained excellent fits for $\xi > 2$ μm (fig. S4). From the cooling length $\xi > 2$ μm, we estimated a lower bound of the hot carrier cooling time $\tau \approx C_{el} \cdot \xi^2/\kappa \approx$ 100 ps, where $C_{el}$ is the electronic heat capacity and $\kappa$ is the thermal conductivity of graphene (*14*). This cooling time is consistent with very slow cooling dynamics recently observed in graphene (*23*). The dimensions of the device allow us to establish only a lower bound for the cooling length. In contrast, other scattering mechanisms, such as optical phonon scattering, occur on far shorter time scales of ~1 ps (*22*, *23*) and are ineffective at cooling low-energy carriers.

Graphene's intrinsic photoresponse also exhibits charge density dependence that confirms hot carrier–assisted transport of thermal energy. For excitation fixed at the p-n interface, the steady state value of $\Delta T$ (*14*) at the laser spot is determined (in the limit of long cooling length) by

$$\Delta T = \frac{dQ/dt}{K_1 + K_2} \qquad (3)$$

where $dQ/dt$ is the rate of heat entering the system, and $K_1$ and $K_2$ are respectively the electronic contributions to the thermal conductance of regions 1 and 2. Because hot carriers proliferate throughout the system, the Wiedemann-Franz relation, $K = \pi^2 k_B^2 T/3e^2 \times (1/R)$, holds. As a consequence, $\Delta T \propto 1/K \propto R$ (*24*). To isolate the density dependence of $\Delta T$, we take the ratio of the photovoltage $V_{PH}$ to the thermovoltage $V_T$ obtained from a fixed temperature difference (*14*). This ratio, $V_{PH}[\mathbf{N}_B]/V_T \propto \Delta T$, is shown in Fig. 3C and clearly exhibits a density dependence that mimics the device resistance. The strong density dependence peaking at the CNP clearly demonstrates the electronic origin of $\Delta T$.

Transport of hot electronic carriers results in a novel nonlocal transport regime that may enable increased power conversion efficiency in energy-harvesting devices. At present, graphene is considered to be an excellent candidate for energy-harvesting optoelectronics, in part because of the presence of high-responsivity photodetection with high internal quantum efficiency (*6*, *9*). Here, we have shown that hot carriers dominate the intrinsic photoresponse and have

demonstrated devices with Seebeck coefficients as high as 12 μV/K (at $T = 40$ K) and high electronic temperature $\Delta T \sim 4.5$ K (*14*). Hot carrier–assisted photoresponse is predicted to improve the power conversion efficiency of energy-harvesting devices beyond standard limits (*29*). Our findings, together with new design principles for next-generation solar thermoelectric devices (*30*), make graphene-based systems viable for energy-harvesting applications.


**References and Notes**

1. S. M. Sze, *Physics of Semiconductor Devices* (Wiley, London, ed. 2, 1981).
2. V. Sukhovatkin, S. Hinds, L. Brzozowski, E. H. Sargent, *Science* **324**, 1542 (2009).
3. N. M. Gabor, Z. Zhong, K. Bosnick, J. Park, P. L. McEuen, *Science* **325**, 1367 (2009).
4. R. Bistritzer, A. H. MacDonald, *Phys. Rev. Lett.* **102**, 206410 (2009).
5. T. Winzer, A. Knorr, E. Malic, *Nano Lett.* **10**, 4839 (2010).
6. J. C. Song, M. S. Rudner, C. M. Marcus, L. S. Levitov, *Nano Lett.* 10.1021/nl202318u (2011).
7. E. J. Lee, K. Balasubramanian, R. T. Weitz, M. Burghard, K. Kern, *Nat. Nanotechnol.* **3**, 486 (2008).
8. J. Park, Y. H. Ahn, C. Ruiz-Vargas, *Nano Lett.* **9**, 1742 (2009).
9. F. Xia, T. Mueller, Y. M. Lin, A. Valdes-Garcia, P. Avouris, *Nat. Nanotechnol.* **4**, 839 (2009).
10. T. Mueller, F. Xia, P. Avouris, *Nat. Photonics* **4**, 297 (2010).
11. G. Nazin, Y. Zhang, L. Zhang, E. Sutter, P. Sutter, *Nat. Phys.* **6**, 870 (2010).
12. X. Xu, N. M. Gabor, J. S. Alden, A. M. van der Zande, P. L. McEuen, *Nano Lett.* **10**, 562 (2010).
13. M. C. Lemme *et al.*, *Nano Lett.* 10.1021/nl2019068 (2011).
14. See supporting material on *Science* Online.
15. B. Huard *et al.*, *Phys. Rev. Lett.* **98**, 236803 (2007).
16. J. R. Williams, L. Dicarlo, C. M. Marcus, *Science* **317**, 638 (2007).
17. B. Özyilmaz *et al.*, *Phys. Rev. Lett.* **99**, 166804 (2007).
18. E. H. Hwang, E. Rossi, S. Das Sarma, *Phys. Rev. B* **80**, 235415 (2009).
19. P. Wei, W. Bao, Y. Pu, C. N. Lau, J. Shi, *Phys. Rev. Lett.* **102**, 166808 (2009).
20. Y. M. Zuev, W. Chang, P. Kim, *Phys. Rev. Lett.* **102**, 096807 (2009).
21. J. Checkelsky, N. P. Ong. *Phys. Rev. B* **80**, 081412(R) (2009).
22. D. Sun *et al.*, *Phys. Rev. Lett.* **101**, 157402 (2008).
23. J. H. Strait *et al.*, *Nano Lett.* 10.1021/nl202800h (2011).
24. N. W. Ashcroft, N. D. Mermin, *Solid State Physics* (Thomson Learning Inc., London, 1976).
25. In the top-gated region, both $V_{BG}$ and $V_{TG}$ contribute to $n_c$, resulting in the slope of the diagonal line $m = \Delta V_{TG}/\Delta V_{BG} = C_{BG}/C_{TG} \approx 0.05$, where $C_{BG}$ and $C_{TG}$ are respectively the bottom- and top-gate capacitances to graphene. $\mathbf{N}_B$ and $\mathbf{N}_T$ in the Fourier transform are perpendicular to the minimum resistance lines (gray dashed lines) in Fig. 2A.
26. E. McCann, *Phys. Rev. B* **74**, 161403 (2006).
27. T. Ohta, A. Bostwick, T. Seyller, K. Horn, E. Rotenberg, *Science* **313**, 951 (2006).
28. E. V. Castro *et al.*, *Phys. Rev. Lett.* **99**, 216802 (2007).
29. R. T. Ross, A. J. Nozik, *J. Appl. Phys.* **53**, 3813 (1982).
30. D. Kraemer *et al.*, *Nat. Mater.* **10**, 532 (2011).



**Acknowledgments:** We thank M. Baldo, P. McEuen, P. Kim, and A. Yacoby for valuable discussions. Supported by the Air Force Office of Scientific Research, a NSF Early Career Award (P.J.H.), and the Packard Foundation. Sample fabrication was performed at the NSF-funded MIT Center for Materials Science and Engineering and Harvard Center for Nanoscale Science.


**Supporting Online Material**

www.sciencemag.org/cgi/content/full/science.1211384/DC1
Materials and Methods
SOM Text
Figs. S1 to S4
References (*31*–*38*)


19 July 2011; accepted 26 September 2011
Published online 6 October 2011;
10.1126/science.1211384


# The Pace of Shifting Climate in Marine and Terrestrial Ecosystems


**Michael T. Burrows,[1]* David S. Schoeman,[2,3] Lauren B. Buckley,[4] Pippa Moore,[5,6] Elvira S. Poloczanska,[7] Keith M. Brander,[8] Chris Brown,[7,9] John F. Bruno,[4] Carlos M. Duarte,[10,11] Benjamin S. Halpern,[12] Johnna Holding,[11] Carrie V. Kappel,[12] Wolfgang Kiessling,[13] Mary I. O'Connor,[14] John M. Pandolfi,[15] Camille Parmesan,[16] Franklin B. Schwing,[17] William J. Sydeman,[18] Anthony J. Richardson[7,9,19]**



Climate change challenges organisms to adapt or move to track changes in environments in space and time. We used two measures of thermal shifts from analyses of global temperatures over the past 50 years to describe the pace of climate change that species should track: the velocity of climate change (geographic shifts of isotherms over time) and the shift in seasonal timing of temperatures. Both measures are higher in the ocean than on land at some latitudes, despite slower ocean warming. These indices give a complex mosaic of predicted range shifts and phenology changes that deviate from simple poleward migration and earlier springs or later falls. They also emphasize potential conservation concerns, because areas of high marine biodiversity often have greater velocities of climate change and seasonal shifts.


Climate warming is a global threat to biodiversity (*1*). Key mechanisms allowing species to cope with warming include shifting biogeographic ranges and altering phenology (the synchronous timing of ecological events) (*2*, *3*) to accommodate spatial and seasonal changes in ambient temperature. Considerable variation in species responses exists: Average range shifts have been reported as 6.1 km/decade for terrestrial communities (*2*), from 1.4 to 28 km/decade for marine communities (*4*), and 16.1 km/decade for a combination of both (*5*), whereas spring phenology has been reported as advancing on average by 2.3 to 2.8 days/decade on land (*2*, *6*) and by 4.3 days/decade at sea (*3*, *7*). One reason for variability in estimates of responses could be that patterns of climate change are dynamic and highly heterogeneous across Earth. Different regions are warming or even cooling at different rates, and air temperatures are rising faster than those of upper ocean waters (*8*), so uniform responses across the globe to climate change should not be anticipated. Instead, organism responses are expected to track the rate of isotherm migration over space and seasons to maintain their thermal niches (*9*, *10*).

Although organisms may respond to aspects of climate change other than temperature, our aim was to generate predictions for shifts in distribution and phenology from physical descriptions of the global thermal environment, and to compare predictions among regions across the land and ocean. We used global surface temperatures (*11*, *12*) over 50 years (1960–2009) to calculate the distribution of the velocity and seasonal shifts of isotherm migration over land and ocean on a 1°-by-1° grid (*7*). The velocity of climate change (*10*) (in km/year) was calculated as the ratio of the long-term temperature trend (in °C/year)


[1]Department of Ecology, Scottish Association for Marine Science, Scottish Marine Institute, Oban, Argyll, PA37 1QA, Scotland, UK. [2]Environmental Sciences Research Institute, School of Environmental Sciences, University of Ulster, Coleraine, BT52 1SA, Northern Ireland. [3]Department of Zoology, Post Office Box 77000, Nelson Mandela Metropolitan University, Port Elizabeth, 6031, South Africa. [4]Department of Biology, University of North Carolina at Chapel Hill, Chapel Hill, NC 27599, USA. [5]Institute of Biological, Environmental and Rural Sciences, Aberystwyth University, Aberystwyth, SY23 3DA, UK. [6]Centre for Marine Ecosystems Research, Edith Cowan University, Perth, 6027, Australia. [7]Climate Adaptation Flagship, Commonwealth Scientific and Industrial Research Organisation Marine and Atmospheric Research, Ecosciences Precinct, General Post Office Box 2583, Brisbane, Queensland 4001, Australia. [8]National Institute of Aquatic Resources, Technical University of Denmark, Charlottenlund Slot, Jægersborg Allé 1, Charlottenlund, Denmark. [9]School of Biological Sciences, University of Queensland, Brisbane, Queensland 4072, Australia. [10]The University of Western Australia Oceans Institute, University of Western Australia, 35 Stirling Highway, Crawley 6009, Australia. [11]Department of Global Change Research, Instituto Mediterráneo de Estudios Avanzados (Consejo Superior de Investigaciones Científicas, University of the Balearic Islands), Esporles, 07190, Spain. [12]National Center for Ecological Analysis and Synthesis, University of California Santa Barbara, 735 State Street, Suite 300, Santa Barbara, CA 93101, USA. [13]Museum für Naturkunde at Humboldt University, Invalidenstrasse 43, 10115 Berlin, Germany. [14]Department of Zoology and Biodiversity Research Centre, University of British Columbia, Vancouver, Canada V6T 1Z4. [15]School of Biological Sciences, Australian Research Council Centre of Excellence for Coral Reef Studies, University of Queensland, Brisbane, Queensland 4072, Australia. [16]Section of Integrative Biology, 1 University Station C0930, University of Texas, Austin, TX 78712, USA. [17]Southwest Fisheries Science Center, National Oceanic and Atmospheric Administration Fisheries Service, 1352 Lighthouse Avenue, Pacific Grove, CA 93950, USA. [18]Farallon Institute for Advanced Ecosystem Research, Post Office Box 750756, Petaluma, CA 94975, USA. [19]Centre for Applications in Natural Resource Mathematics, School of Mathematics and Physics, University of Queensland, St Lucia, Queensland 4072, Australia.

*To whom correspondence should be addressed. E-mail: michael.burrows@sams.ac.uk